MDPI

Article

A golden-ratio ladder and a delocalisation-saturated participation bridge for the hydrogen-bond network of liquid water

Jonathan Washburn[1] **and Elshad Allahyarov**[1,2,3,4,*]

[1] Recognition Science Research Institute, Austin, TX, USA
[2] Institut für Theoretische Physik II: Weiche Materie, Heinrich-Heine Universität Düsseldorf, Universitätsstraße 1, 40225 Düsseldorf, Germany
[3] Theoretical Department, Joint Institute for High Temperatures, Russian Academy of Sciences (IVTAN), 13/19 Izhorskaya street, Moscow 125412, Russia
[4] Physics Department, Case Western Reserve University, Cleveland, OH 44106-7202, USA
* Correspondence: elshad.allakhyarov@case.edu

Abstract

We organize the ultrafast hydrogen-bond timescales and the far-infrared/terahertz intermolecular band centres of liquid water on a single discrete golden-ratio ladder, anchored to the 80 fs H-bond contraction time and indexed by a loop-free tetrahedral Bethe sequence. Both the time-domain timescales and the principal frequency-domain bands fall inside the rung windows set by their shell index, placing the two data sets on one spacing from one time anchor. A separate empirical energy anchor gives a two-parameter calibrated map of freezing and density maximum. A TIP4P/Ew analysis shows that participation is delocalisation-saturated rather than linear in $N(n)$, and we fit a corresponding two-parameter saturating law. The low-frequency intermolecular modes are delocalised over the network, with coherent shell-breathing extending over about one coordination shell — a result stable with temperature. The ladder placements are therefore an organizing construction with explicit calibrations. Together these establish a calibrated, physically interpretable bridge between hydrogen-bond-network topology and vibrational participation, with the ladder supplying the rung spacing and the molecular dynamics supplying the participation law that populates it.

Keywords: liquid water; hydrogen bonding; H-bond network topology; Bethe lattice; golden-ratio ladder; molecular dynamics; TIP4P/Ew; instantaneous normal modes; far-infrared/THz spectroscopy

1. Introduction

The structure and dynamics of liquid water have been studied since the 1930s tetrahedral-network proposals of Bernal–Fowler [1] and Pauling [2], through Stillinger [3] to modern diffraction [4–6] and far-infrared/THz spectroscopy [7–10]. Liquid water is locally close to tetrahedral but its H-bond network contains closed rings, with substantial populations of five- and six-membered H-bond rings [11]. What remains less clear is whether the reported time-domain and frequency-domain features admit a common discrete ordering.

Ultrafast and picosecond hydrogen-bond dynamics provide a reported set of characteristic timescales and intermolecular band peaks, from intramolecular O–H stretch ($\sim$ 10 fs) and H–O–H bend ($\sim$ 1640 cm^{-1} in liquid water, period $\sim$ 20 fs [12]) through H-bond stretch and bend bands at 60–180 cm^{-1} (periods $\sim$ 185–560 fs), picosecond rearrangements,

Received:
Revised:
Accepted:
Published:

and tens-of-picoseconds orientational decorrelation [13–17]. We use these literature values as reported band centres and characteristic timescales, not as unique microscopic mode assignments. In parallel, water shows a cooperative thermodynamic anomaly with the density maximum at 277.15 K and a first-order freezing transition at 273.15 K.

Existing descriptions of liquid-water dynamics usually address one observable class at a time: INM studies analyse vibrational eigenvectors and mode localisation [18,19, 39], empirical and machine-learned potentials provide simulation Hamiltonians [20–22], phonon-like analyses describe propagating collective modes [40], and two-state or two-liquid models target thermodynamic anomalies [23–25]. The present work asks a different, more limited question: whether the time-domain H-bond processes [13,15–17] and the far-IR/THz bands [9,10,26] can be placed on one externally fixed discrete ladder, and whether the corresponding participation content can be measured directly in MD.

For the near-freezing anomaly specifically, percolation models [27,28], locally favoured structures [24,25], and two-liquid pictures [23,29–31] provide the relevant thermodynamic context. The temperature map below is therefore presented as a calibrated ladder relation, not as a replacement equation of state.

The model developed below uses these literatures in a specific division of roles: ultrafast and THz experiments supply the timescale and band inputs [13–17,32,33]; graph theory supplies the loop-free shell count tested against the H-bond graph [11,38]; and INM analysis supplies the participation measurement used to populate the ladder dynamically [18,19,39,40].

This paper pursues three linked aims. Aim 1 places the reported ultrafast H-bond timescales and the principal far-IR/THz bands on the rung windows of the ladder $\tau_n = \tau_0 \varphi^n$, indexed by the loop-free Bethe shell sizes $N(n)$. Aim 2 uses the same ladder, with one time anchor and one empirical energy anchor, to construct a calibrated map of the freezing and density-maximum temperatures. Aim 3 tests the dynamical content of the shell assignment by measuring, in liquid water, how many molecules share each low-frequency vibration. These aims deliberately separate organization from prediction: the bracketing is not claimed to prove uniqueness of φ, and the thermodynamic map is treated as calibrated.

The remaining part of the paper is organized to follow these three aims in turn. Sec. 2 defines the algebraic inputs, the physical bridges, and the two calibration anchors. In Sec. 3 we develop Aim 1. Sec. 4 develops Aim 2, and Sec. 5 develops Aim 3. In Sec. 6 we discuss open questions and outlook. We conclude in Sec. 7.

2. Model Construction

2.1. Input parameters

Table 1 collects the recurring symbols used in the model and in the MD tests.

Our model invokes two algebraic parameters. The first is the ladder spacing golden ratio parameter $\varphi = (1 + \sqrt{5})/2$, The value φ is an external input: it is fixed by the separate theoretical framework of Refs. [41–45]. Everything below tests how well water's timescales are organized by this externally fixed spacing; it does not claim that the data single out φ over alternative logarithmic bases. It defines the discrete timescale ladder

$$\tau_n = \tau_0 \, \varphi^n \tag{1}$$

where τ_n is the characteristic timescale (the logarithmic "period") assigned to rung n of the ladder, and τ_0 is the unit/base timescale (the rung-0 period), which sets the absolute scale.

The second input parameter is the cumulative Bethe-lattice shell sizes sequence,

$$N(n) = 1 + z \sum_{k=0}^{n-1} (z-1)^k = 2 \cdot 3^n - 1 \tag{2}$$

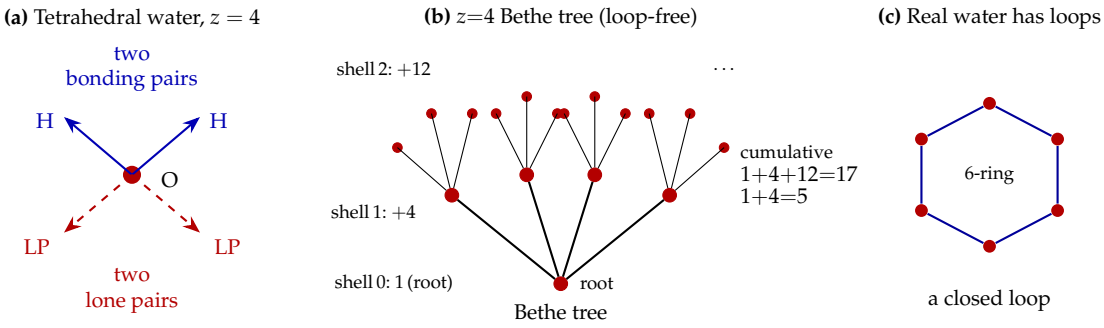

Figure 1. Schematic of the model's structural input. **(a)** Tetrahedral water with two donor bonds and two lone-pair acceptor directions. **(b)** The corresponding loop-free $z = 4$ Bethe-tree idealisation; layer counts $1+4+12 = 17$ are the cumulative shell sizes that enter Eq. (2) at $z = 4$ (this is $N(2) = 17$ in the sequence of Eq. (3)). **(c)** A 6-membered H-bond ring, illustrating the loop structure absent from the Bethe lattice.

evaluated at the ideal tetrahedral valence $z = 4$ [5,6]. It is the local valence of the loop-free reference graph, used because an isolated water molecule has two donor and two acceptor H-bond directions. The tetrahedral local geometry is illustrated in Fig. 1(a) and feeds directly into the branching number $z - 1 = 3$ of the loop-free Bethe reference. In Eq.(2) $N(n)$ is the total number of vertices reachable from a chosen root within n H-bond steps, including the root itself and all preceding shells. Equation (2) is the cumulative shell count for a rooted neighbourhood of the infinite z-regular Bethe lattice. A finite rooted tree with the same branching is often called a Cayley tree. Here we use only the local, loop-free shell counts, not boundary properties of a finite tree. For $n = 0, \ldots, 7$ this yields the sequence

$$N(n) \in \{1, 5, 17, 53, 161, 485, 1457, 4373\}. \tag{3}$$

Table 1. Nomenclature for the main quantities used in the model and tests.

Symbol	Meaning	Where it enters
φ	Golden-ratio spacing, $(1+\sqrt{5})/2$	Ladder definition, Eq. (1)
n	Integer rung or Bethe-shell index	Rung windows and shell depth
τ_0	Base timescale fixed by the 80 fs anchor, $\tau_0 = 80\,\text{fs} \cdot \varphi^{-5} \approx 7.2\,\text{fs}$	Eq. (1)
τ_n	Period assigned to rung n	$\tau_n = \tau_0 \varphi^n$
z	Ideal local H-bond valence	$z = 4$
$N(n)$	Loop-free cumulative Bethe-shell size	Eq. (2) and Table 2
N_{eff}	Effective participation number	Eq. (4)
P_k	INM participation ratio of mode k	Dynamical test, Table 4
$N_{\text{MD}}(n)$	Measured cumulative BFS neighbour reach in the H-bond graph	Topological test, Sec. 5.2
E_{coh}	Empirical energy anchor, φ^{-5} eV	Sec. 4
T_c	Cooperative-transition temperature bracket	Eq. (14)
T_{max}	Density-maximum temperature bracket	Eq. (15)

2.2. Participation number N_{eff}

We introduce the *effective participation number* N_{eff} as a standard inverse-participation-ratio (IPR) measure of how many molecules carry significant amplitude in a vibrational mode. For a normalised eigenvector with components u_i on molecule i ($\sum_i u_i^2 = 1$),

$$N_{\text{eff}} \equiv \frac{(\sum_i u_i^2)^2}{\sum_i u_i^4} = \frac{1}{\sum_i u_i^4}, \tag{4}$$

This equation gives $N_{\text{eff}} = 1$ for a mode localised on one molecule, $N_{\text{eff}} = N_{\text{tot}}$ for a mode spread uniformly over the whole box, and $N_{\text{eff}} = k$ for an ideal mode equally shared by k molecules. The INM test of Sec. 5.3 evaluates this same quantity on mass-weighted Hessian eigenvectors $\{v_k\}$ as

$$P_k = \frac{1}{\sum_i v_{ki}^4}, \tag{5}$$

so N_{eff} and P_k are the same participation measure, used respectively for the model assignment and the simulated eigenvectors. We assume that the shell-n participation number equals the Bethe shell size,

$$N_{\text{eff}}(n) = N(n) = 2 \cdot 3^n - 1, \tag{6}$$

and call the corresponding idealised oscillation the *shell-n vibration*: a chosen central molecule and its first n H-bond shells are assumed to move in phase. For shells beyond the first neighbour cage this is a formal model construct, not a claim that hundreds of molecules in the disordered liquid execute a compact in-phase breathing motion. The MD test below is included precisely to determine where that compact-coherence picture breaks down. This assumption is tested directly against the molecular-dynamics participation data in Sec. 5.3.

Real liquid water differs from the loop-free Bethe idealisation in two ways: it has loops (the 5- and 6-membered rings noted in the Introduction) and finite correlation lengths. The Bethe lattice is therefore retained only as the loop-free topological reference for local tetrahedral branching, not as a literal structural model. Figure 1 illustrates the model: panel (a) the molecular geometry, panel (b) the resulting Bethe tree with layer counts $1+4+12 = 17$, and panel (c) a 6-membered ring that is forbidden in the Bethe lattice but present in real water.

2.3. Calibration anchors

Two empirical anchors fix the absolute scales used in this paper: a time anchor for the spectroscopic ladder and an energy anchor for the temperature map.

First, the reported ~ 80 fs H-bond contraction time of liquid water [13,15,17] sets the unit timescale

$$\tau_0 = 80\,\text{fs} \cdot \varphi^{-5} \tag{7}$$

Anchoring rung 5 (rather than another integer rung) is a labelling convention only: the ladder $\tau_n = \tau_0\,\varphi^n$ is invariant under $n \to n + k$ together with $\tau_0 \to \tau_0\,\varphi^{-k}$, so only the inter-rung gaps between successive assigned timescales are physical. Appendix B checks the shell-1 H-bond stretching assignment in TIP4P/Ew water. Because the sub-100 fs water response is obtained from multi-exponential spectroscopic fits and can mix spectral diffusion, librational, and structural components, the 80 fs value is used here as a literature anchor with uncertainty rather than as a sharp microscopic constant. The operational consequences of the anchor (rung-offset formula, rung-assignment criterion) are developed in Sec. 2.4(d).

Second, as an empirical energy anchor we set

$$E_{\text{coh}} \equiv \varphi^{-5}\,\text{eV} \approx 0.0902\,\text{eV}, \tag{8}$$

Assigning the unit electronvolt to the dimensionless φ^{-5} is a chosen convention. we adopt it because the resulting value (≈ 0.09 eV) sits near the low end of the measured per-bond H-bond enthalpy range $[0.08, 0.30]$ eV [46–48], and we quantify below how the temperature

mapping depends on this choice. The dependence of the freezing-point bracket on this choice is quantified in Sec. 4.

2.4. *Vibrational timescale* τ

This subsection discusses a connection between the participation number N_{eff} and the vibrational timescale τ, and then states how individual timescales and whole Bethe shells are assigned to integer rungs of the φ-ladder. It proceeds in four steps: (a) the two physical assumptions; (b) the period law $\tau \propto \sqrt{N_{\text{eff}}}$ derived from them; (c) the consequence of combining that law with the bridge $N_{\text{eff}}(n) = N(n)$; and (d) the rung-assignment criterion and the Bethe-shell windows it produces. The assumptions are therefore part of the ideal ladder construction. They are not assumed to survive unchanged in the real liquid. Sec. 5.3 measures the actual participation and shows that the equal-amplitude compact-cluster reading is replaced by a saturated, delocalised one.

(a) Assumptions.

The shell-n vibration is modelled as a coherent harmonic oscillation under two assumptions. (i) All N_{eff} molecules share a single collective coordinate $X(t)$ and oscillate with equal displacement amplitude ($u_i = 1/\sqrt{N_{\text{eff}}}$ for all i, and hence equal velocity amplitude $\dot{X}$). (ii) The restoring stiffness of that coordinate is a shell-independent effective H-bond stiffness k, with no N_{eff}-dependent renormalisation. Assumption (i) is more restrictive than the general IPR definition of Sec. 2.2: for non-uniform amplitudes the effective mass is smaller than $N_{\text{eff}}\, m$ (the most-active molecules dominate), so $\tau \propto \sqrt{N_{\text{eff}}}$ is then only a period *upper bound*; under the equal-amplitude assumption (i) the inequality becomes an equality and $\tau \propto \sqrt{N_{\text{eff}}}$ is exact within the model.

(b) Period scaling $\tau \propto \sqrt{N_{\text{eff}}}$.

Under assumption (i) the total kinetic energy is

$$\text{KE} = \tfrac{1}{2} \sum_{i=1}^{N_{\text{eff}}} m\, \dot{x}_i^2 = \tfrac{1}{2} \left(N_{\text{eff}}\, m\right) \dot{X}^2, \tag{9}$$

so the effective mass of the collective coordinate is the sum of the individual molecular masses,

$$M_{\text{eff}} = N_{\text{eff}}\, m \;\propto\; N_{\text{eff}}, \tag{10}$$

where $m = m_{\text{H}_2\text{O}} = 18.015\,\text{amu}$. With the shell-independent stiffness k of assumption (ii), Newton's equation for X reads

$$M_{\text{eff}}\, \ddot{X} = -k\, X, \tag{11}$$

giving an angular frequency $\omega = \sqrt{k/M_{\text{eff}}}$ and a period

$$\tau \;=\; \frac{2\pi}{\omega} \;=\; 2\pi \sqrt{\frac{N_{\text{eff}}\, m}{k}} \;=\; \sqrt{N_{\text{eff}}} \cdot \tau_{\text{single}}, \qquad \tau_{\text{single}} \equiv 2\pi\sqrt{m/k}. \tag{12}$$

We take this as the working scaling of the model:

$$\tau \propto \sqrt{N_{\text{eff}}}. \tag{13}$$

(c) Shell-vibration assignment and the per-rung gap.

Combining part (b) with the participation-bridge identification Eq. (6) gives $\tau_n \propto \sqrt{N(n)}$, whose shell-to-shell growth is close to, but not exactly, the φ-ladder spacing. The size of this near-coincidence is definite. Because the shell sizes grow as $N(n) = 2 \cdot 3^n - 1 \sim 3^n$, successive shells differ by the branching factor $z - 1 = 3$, so the period law $\tau \propto \sqrt{N(n)}$

gives an asymptotic period ratio $\tau_{n+1}/\tau_n = \sqrt{N(n+1)/N(n)} \to \sqrt{3} \approx 1.732$ per shell, while the ladder spaces by $\varphi \approx 1.618$ per rung. The residual per-step factor $\sqrt{3}/\varphi \approx 1.071$ accumulates to $(\sqrt{3}/\varphi)^8 \approx 1.73$ over eight shells and to $\sqrt{N(8)}/\varphi^8 \approx 2.4$ across the reported set. A single-rung-wide (point) ladder would require a reference sequence whose growth rate is exactly φ^2 per shell, so that $\sqrt{N(n+1)/N(n)} \to \varphi$; the $z = 4$ Bethe sequence does not have this growth rate, and we keep $z = 4$ because it is fixed by the tetrahedral chemistry. The consequence is that each Bethe shell is bracketed by a two-rung-wide window rather than a single rung—only shell 0 lands on one rung, since $N(0) = 1 = \varphi^0$. Each shell should therefore be read as falling within a two-rung-wide band of the ladder, not as hitting a single sharp φ^n value.

(d) Rung-assignment criterion and Bethe-shell windows.

The ladder is anchored at $\tau_0 = 80\,\text{fs} \cdot \varphi^{-5} \approx 7.2\,\text{fs}$. We state here the rung-assignment criterion that compares individual timescales and Bethe-shell sizes to the ladder.

The rung offset of a mode with participation number N_{eff} relative to rung 5 follows from Eq. (13) and the calibration $\tau(N_{\text{eff}} = 1) = \tau_0\varphi^5$: since $\tau \propto \sqrt{N_{\text{eff}}}$ and $\tau \propto \varphi^n$, the rung shift satisfies $\varphi^{\Delta r} = \sqrt{N_{\text{eff}}}$, giving $\Delta r = \frac{1}{2}\log_\varphi N_{\text{eff}}$.

We adopt the following formal rung-assignment criterion: a measured timescale τ_{obs} is said to be *assigned to rung n* if $\tau_{\text{obs}} \in [\tau_0\,\varphi^{n-1/2},\ \tau_0\,\varphi^{n+1/2})$, i.e. if its log-period satisfies $|\log_\varphi(\tau_{\text{obs}}/\tau_0) - n| < 1/2$. This gives each rung a multiplicative window of width $\varphi \approx 1.62$ in period, with a half-rung tolerance of $\sqrt{\varphi} \approx 1.27$ (about $\pm 27\%$) around the centre. The tolerance is wide, so the bracketing claim is qualitative. This nearest-integer rule defines what we mean by "a rung match". Note that the Bethe-shell windows span two rungs because each $N(n)$ lies between two consecutive φ powers; the half-rung criterion applies to individual observed timescales, not to the Bethe-shell brackets.

Each Bethe shell size $N(n)$ is then bracketed by consecutive φ powers, $\varphi^a < N(n) < \varphi^b$, and Eq. (13) places the predicted integer rung in the window $[5 + \lfloor a/2 \rfloor,\ 5 + \lceil b/2 \rceil]$. Concretely: $\varphi^3 < 5 < \varphi^4$ (shell 1 $\to$ rungs 6–7); $\varphi^8 < 53 < \varphi^9$ (shell 3 $\to$ rungs 9–10); $\varphi^{12} < 485 < \varphi^{13}$ (shell 5 $\to$ rungs 11–12); these are the three THz-matching windows tabulated and discussed in Sec. 3.1. Steps (a)–(d) thus turn the algebraic inputs of Sec. 2 into a candidate timescale ladder for liquid water.

3. Rung bracketing of the H-bond hierarchy

This section brackets the reported H-bond timescale hierarchy and the principal far-infrared/THz band centres against the discrete logarithmic ladder $\tau_n = \tau_0\,\varphi^n$ of Sec. 2. Periods and wavenumbers are related by $\tau = 1/(\tilde{\nu}c)$, equivalently $\tau\tilde{\nu} = 1/c \approx 33{,}356\,[\text{fs}]/[\text{cm}]$. The master rung table is Table 2; the graphical summary is Fig. 2.

3.1. Master rung table and consistency checks against the data

Applying the rung-bracketing rule of Sec. 2.4 to the eight Bethe-shell sizes $N(n) = 2 \cdot 3^n - 1$ ($n = 0, \ldots, 7$) yields the master rung table (Table 2). Each row gives one shell, its φ bracket, the predicted integer rung window, the predicted period and wavenumber range, and the independent literature measurement that falls in that window. The rung-5 row (shell 0, $N_{\text{eff}} = 1$) is the calibration anchor τ_0 and is fixed by construction. The remaining rows are calibration-free placements on the same ladder; they show how the reported H-bond timescales and band centres align with the Bethe-indexed rung windows, while their statistical status is discussed after Fig. 2.

The entries in Table 2 fall into three classes:

Table 2. $z = 4$ Bethe-lattice shells with predicted rung ranges and experimental matches across both ultrafast (time-domain) and THz/far-IR (frequency-domain) sets. Entries in the "Pred. rung", "Pred. $\tilde{\nu}$", and "Pred. τ" columns are derived from Eq. (2) (Bethe shell size $N(n)$), Eq. (13) (the $\tau \propto \sqrt{N_{\text{eff}}}$ scaling), and the rung-5 calibration anchor (80 fs). The "Experimental match" column lists independent literature measurements [7–10,13–15,17]. The φ-bracket column uses open intervals (φ^a, φ^b). This table reports calibration-free placements on the ladder; the statistical status of these placements is stated after Fig. 2.

Shell	$N(n)$	φ bracket	Pred. rung	Pred. $\tilde{\nu}$ (cm^{-1})	Pred. τ	Experimental match (cm^{-1}; τ)
0	1	φ^0	5	417	80 fs	*calibration anchor*: rung 5 $\equiv$ 80 fs $\equiv$ 417 cm^{-1}
1	5	(φ^3, φ^4)	6–7	160–260	129–209 fs	**THz H-bond stretch**: $\sim$180 cm^{-1}; $\sim$185 fs
2	17	(φ^5, φ^6)	7–8	100–160	209–339 fs	ultrafast vibr. relaxation: 111 cm^{-1}; 300 fs
3	53	(φ^8, φ^9)	9–10	38–61	549–887 fs	**THz H-bond bend**: $\sim$60 cm^{-1}; $\sim$555 fs
4	161	$(\varphi^{10}, \varphi^{11})$	10–11	24–40	0.89–1.44 ps	ultrafast H-bond breaking: 33 cm^{-1}; 1 ps
5	485	$(\varphi^{12}, \varphi^{13})$	11–12	15–24	1.44–2.33 ps	**THz low-freq. connectivity**: $\lesssim$ 30 cm^{-1}; $\gtrsim$ 1.1 ps
6	1457	$(\varphi^{15}, \varphi^{16})$	12–13	9–15	2.33–3.76 ps	ultrafast molecular jump: 13 cm^{-1}; 2.5 ps
7	4373	$(\varphi^{17}, \varphi^{18})$	13–14	6–9	3.76–6.09 ps	ultrafast freq. decorrelation: 6.7 cm^{-1}; 5 ps

(i) **THz/far-IR bands**: the three principal intermolecular bands of liquid water are associated with the three odd-numbered Bethe shells 1, 3, and 5, namely the H-bond stretch, H-bond bend, and low-frequency connectivity band [7–10].

(ii) **Ultrafast and picosecond timescales**: shells 2, 4, 6, and 7 bracket the reported H-bond relaxation processes from hundreds of femtoseconds to several picoseconds [13–15,17].

(iii) **One outside-shell rung**: rung 18 carries the network orientational decorrelation (50 ps), the slowest reported H-bond timescale. Numerical placements for the intramolecular O–H stretch and H–O–H bend are recorded separately in Appendix A.

The eight Bethe shells span rungs 5–14 of the ladder (about six octaves of timescale). The graphical summary on a logarithmic rung axis is Fig. 2.

The rung axis of Fig. 2 is not uniformly filled: a bare rung separates the shell-2 and shell-3 windows. This follows directly from the period law $\tau \propto \sqrt{N_{\text{eff}}}$, which places a shell at rung $5 + \frac{1}{2}\log_\varphi N(n)$. A shell would fall on rungs 8–9 only if its size lay in the interval $\varphi^6 \approx 18 < N < \varphi^8 \approx 47$; but the Bethe shells grow by a factor of three per step, so shell 2 has $N = 17$ (just below φ^6, rungs 7–8) and shell 3 has $N = 53$ (just above φ^8, rungs 9–10). The size jumps straight from 17 to 53, stepping over the whole $[18, 47]$ range that brackets $\varphi^7 \approx 29$, so no shell lands near rung 8.5 and that rung stays empty. The gap is the per-rung mismatch of Sec. 2.4(c) seen graphically: each shell advances the window centre by only $\frac{1}{2}\log_\varphi 3 \approx 1.14$ rungs, but because $N(n)$ grows in discrete $\times 3$ jumps the bracket exponents step $5 \to 6 \to 8 \to 9 \to \cdots$ and occasionally skip a φ-power. The shell-3 to shell-6 windows happen to abut without skipping an integer rung, so the gap appears only between shells 2 and 3.

Using the half-rung criterion of Sec. 2.4(d), the model brackets the timescale set but does not predict exact φ^n ratios. The seven non-anchor rung assignments have mean $|\text{deviation}| \approx 14\%$ and maximum $\approx 20\%$ (rung 18, 50 ps). Table 2 and Fig. 2 therefore establish a bounded placement result: the reported timescales and band centres fall inside

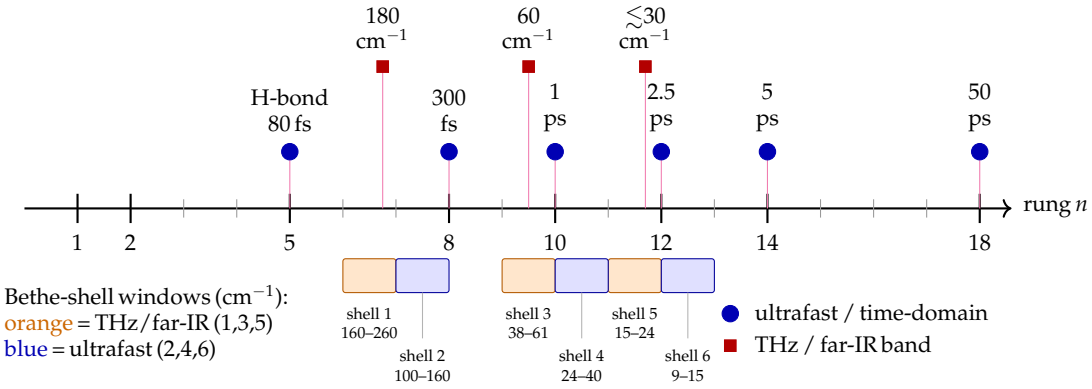

Figure 2. Rung-ladder map of the water timescale set. Integer rungs are logarithmic periods $\tau_n = \tau_0 \varphi^n$ relative to the 80 fs calibration at rung 5. Circles mark time-domain Bethe-shell assignments, squares mark THz/far-IR Bethe-shell bands, orange windows show the THz/far-IR Bethe-shell ranges (odd shells 1, 3, 5), and blue windows show the ultrafast Bethe-shell ranges (even shells 2, 4, 6). The intramolecular O–H stretch and H–O–H bend are intramolecular vibrations, not shell-n network modes of the Bethe construction, and are excluded from this figure and from all ladder-performance claims (see Appendix A).

their assigned rung windows from one time anchor, while the window widths, anchor uncertainty, and retrospective band assignments mean that this bracketing is not by itself a statistical proof of the ladder or a model-selection result against nearby logarithmic bases.

Sensitivity to the anchor. The 80 fs contraction time is itself a model-dependent quantity, extracted from multi-exponential fits to 2D-IR spectral-diffusion and photon-echo data and conflating several sub-100 fs processes, with a realistic spread of order ± 20 fs ($\pm 25\%$) [13,17]. Because of the relabelling invariance noted in Sec. 2.3, changing the anchor leaves the inter-rung gaps unchanged but shifts all absolute rung labels. A $\pm 25\%$ shift in τ_0 corresponds to $\Delta r = \log_\varphi(1.25) \approx 0.46$ rungs, about half a rung, so assignments near a window edge can move by one full integer label under the stated anchor uncertainty. Consequently the integer labels in Table 2 should be read as central assignments. The robust statement is the relative ordering of the reported processes across the ladder, whereas any individual edge-case label can shift by roughly one rung under the anchor envelope.

4. Cooperative-transition and density-maximum mapping

This section uses the energy anchor E_{coh} of Eq. (8) to build a calibrated temperature map. The map has two targets: a cooperative-transition temperature T_{c} near the freezing point and a density-maximum temperature T_{max} near $T_{\mathrm{obs}} = 277.15\,\mathrm{K}$. The resulting values, $T_{\mathrm{c}} = 271.8\,\mathrm{K}$ and $T_{\mathrm{max}} = 277.6\,\mathrm{K}$, are therefore reported as calibrated matches to $T_{\mathrm{freeze}} = 273.15\,\mathrm{K}$ and T_{obs}, not as independent thermodynamic predictions. The section is retained only as a phenomenological extension of the ladder. It is not used as evidence for the spectroscopic bracketing or for the MD participation result.

For T_{c} we use an Arrhenius-style calibration in which the energy scale E_{coh} is divided by n logarithmic ladder steps of size $\ln\varphi$,

$$T_{\mathrm{c}} \;=\; \frac{E_{\mathrm{coh}}}{n\,k_{\mathrm{B}}\,\ln\varphi} \;=\; \frac{\varphi^{-5}\,\mathrm{eV}}{8\,k_{\mathrm{B}}\,\ln\varphi} \;\approx\; 271.8\,\mathrm{K}, \tag{14}$$

where the integer $n = 8$ is fixed by requiring the formula to reproduce the freezing point; it is a calibration choice, so Eq. (14) is a fit to T_{freeze}.

For the density-maximum temperature T_{max} we adopt a multiplicative shift,

$$T_{\mathrm{max}} \;=\; T_{\mathrm{c}}\,(1+\varphi^{-8}) \;\approx\; 277.6\,\mathrm{K} \tag{15}$$

which gives the observed density-maximum temperature to within about 0.5 K. The exponent 8 is a calibrated shift exponent and is independent of the integer 8 in Eq. (14); we do not assign physical meaning to their numerical equality. A microscopic equation-of-state derivation of Eq. (15) remains an open problem. Because both the eV assignment for E_{coh} and the two integer exponents are selected to match near-freezing landmarks, this construction has no standalone predictive power until tested away from bulk ambient water. A change of E_{coh} over the published H-bond energy range would move T_{c} proportionally, so the numerical agreement should not be read as a derived equation of state. For this reason the falsifiable observable is the dimensionless offset relation rather than the absolute temperatures: without refitting the shift exponent, a measured $(T_{\mathrm{max}} - T_{\mathrm{c}})/T_{\mathrm{c}}$ outside the broad interval $[0.010, 0.035]$ in a modified system would rule out Eq. (15) at the precision claimed here.

5. Molecular-dynamics tests of the participation bridge

The model's participation-number bridge $N_{\mathrm{eff}}(n) = N(n)$ admits two distinct empirical readings: (i) a *topological* reading, in which the cumulative Bethe shell sizes are upper bounds on the breadth-first-search (BFS) reach in the actual H-bond network, and (ii) a *dynamical* reading, in which the same shell sizes are the band-resolved participation ratios P_k at the corresponding intermolecular frequencies. Here BFS is the standard graph traversal that starts from a chosen molecule, visits all of its directly H-bonded neighbours, then all of *their* not-yet-visited neighbours, and so on shell by shell; the BFS reach at step n is the number of distinct molecules reachable within n H-bond hops of the starting molecule, which is exactly the network analogue of the cumulative Bethe shell size $N(n)$. Both readings predict the same band positions, so the rung-bracketing analysis of Sec. 3 alone cannot discriminate them; we need explicit access to the H-bond graph and to the mass-weighted vibrational eigenvectors of liquid water. We obtain both from TIP4P/Ew molecular dynamics. The simulation setup is described in Sec. 5.1, the topological test in Sec. 5.2, the dynamical test in Sec. 5.3, and the two are brought together in Sec. 5.4.

5.1. Setup and simulation protocol

The molecular-dynamics runs used the TIP4P/Ew rigid four-site potential [49] in OpenMM 8.5 [50], with post-processing in NumPy and SciPy [51,52]. All runs use the same two-stage protocol. First, the box is equilibrated in NPT at 1 atm so that the volume relaxes to the ambient liquid density, $\rho \simeq 1.0\,\mathrm{g\,cm^{-3}}$, at the target temperature. Second, the production trajectory is propagated in NVE. This is the appropriate split for vibrational observables: the barostat and thermostat set the state point, but they are removed before measuring low-frequency participation, density-of-states, and velocity-projection signals, where coordinate rescaling or thermostat friction would perturb the dynamics.

The topological BFS test uses an $N = 5000$ system of rigid water molecules in a cubic periodic box at the ambient liquid density ($\rho \simeq 1.0\,\mathrm{g\,cm^{-3}}$), equilibrated at $T = 298$ K (NPT, Monte-Carlo barostat at 1 atm, 100 ps) and then propagated for 250 ps in the NVE ensemble with a Verlet integrator and a 2 fs time step. The dynamical INM participation results reported in the main text use the same NPT-equilibrate/NVE-produce protocol at the ambient density ($\rho \simeq 1.0\,\mathrm{g\,cm^{-3}}$) at two temperatures, 298 and 277 K (Sec. 5.6). Long-range electrostatics used particle-mesh Ewald with an 8.5 Å real-space cutoff. The dynamical INM participation test reported in Table 4 is performed on the same system at 298 K and ambient density. Two complementary INM analyses are used. (i) A *translational* analysis: for each of eight instantaneous thermal configurations sampled at ≥ 20 ps separation along the production trajectory (several times the longest H-bond correlation time of interest, so that they are statistically independent draws), the mass-weighted Hessian of the molecular

centre-of-mass translations (three degrees of freedom per molecule) was assembled by finite-difference of the simulation forces and diagonalised numerically, pooling 120,000 modes. (ii) A *rigid-body* $6N$ cross-check that adds the three molecular rotations per molecule: two configurations were first quenched to a local potential-energy minimum, and the full $6N \times 6N$ mass-weighted Hessian diagonalised (60,000 modes). The TIP4P M virtual site, which carries the molecular charge, is included in every force and torque sum, and its position is recomputed after each finite-difference displacement. Because this $6N$ calculation uses quenched configurations rather than the same eight thermal INM frames, it is treated as a separate delocalisation check, not as statistically identical evidence to the translational-INM analysis. Three numerical checks on the $N = 5000$ box validate the INM calculation: the three acoustic translation modes return to zero (smallest $|\tilde{\nu}| \leq 2.4\,\mathrm{cm}^{-1}$), the density of states peaks at $\sim 160\,\mathrm{cm}^{-1}$ with $\approx 21\%$ modes of imaginary frequency (negative Hessian eigenvalues) (consistent with the INM literature for water), and the band-averaged participations are stable to $\sim 5\%$ over a five-fold range of the finite-difference step.

The H-bond adjacency matrix is constructed under two definitions: the distance-only (DIST: $r(\mathrm{O},\mathrm{O}) < 3.5$ Å) and the Luzar–Chandler angular criterion (ANG: $r(\mathrm{O},\mathrm{O}) < 3.5$ Å and $\angle(\mathrm{H},\mathrm{O}_d,\mathrm{O}_a) < 30°$) [53], giving mean coordination $\langle z\rangle_{\mathrm{DIST}} = 4.73$ and $\langle z\rangle_{\mathrm{ANG}} = 3.63$, respectively. The latter is the canonical liquid-water value ($\sim$ 3.5–3.7) and corresponds to a $\sim 9\%$ broken-bond fraction at 298 K; the two definitions bracket the model assumption $z = 4$. If the Bethe formula is evaluated at the measured mean coordinations rather than at the ideal tetrahedral value, the shell sizes change substantially: for $z = 3.63$, $N(1,3,5,6) \approx (4.6, 39, 279, 736)$, while for $z = 4.73$, $N(1,3,5,6) \approx (5.7, 89, 1250, 4665)$. These values are not used as replacement predictions, because the Bethe construction is deliberately tied to the ideal tetrahedral valence $z = 4$. They show instead that the measured coordination definition is one source of uncertainty in mapping shell depth to reach. Thus the Bethe sequence is a strict reach bound only for the ideal local-valence reference; real-water coordination deficits and ring closure relax that bound and make the shell labels organizational rather than literal MD shell-size predictions.

5.2. Topological test: BFS shell sizes in the H-bond graph

We measure how far the breadth-first search reaches in n steps from a typical molecule in liquid water's actual H-bond graph, and compare it with the loop-free Bethe value $N(n)$. We compute cumulative BFS shell sizes on
(i) two idealised $z = 4$ reference graphs (a diamond-cubic lattice (a regular crystalline $z = 4$ network), and a random graph in which every vertex has exactly four neighbours but the connections are otherwise drawn at random), and
(ii) the TIP4P/Ew H-bond network at $N = 5000$, averaged over all 5000 starting vertices and 50 trajectory frames under both the DIST and ANG H-bond definitions of Sec. 5.1. A depth-7 finite Bethe tree has 4373 vertices and reproduces the ideal cumulative values through shell 7, including shells 5 and 6; thus the Bethe-theory row in Table 3 is not affected by finite-tree saturation over the shell range used here.

Table 3 reports the cumulative reach values. Shell 0 is exact by construction. At shells 1 and 2 the MD values agree with Bethe to within $\sim 17\%$, with DIST slightly above and ANG slightly below. From shell 3 onward the MD values fall progressively below Bethe; at shell 5, both definitions are 2.4–3.5$\times$ below Bethe. The reduction is the expected loop signature: short rings shorten BFS distances and so reduce the n-th reach below the loop-free reference $N(n)$. Under the canonical ANG definition the measured reach falls progressively further below the tree, reaching $\sim 6\times$ below by shell 6; under the DIST definition it is marginally above the tree at shells 1–2 (the distance-only criterion over-counts near oxygen neighbours) and $\sim 4\times$ below by shell 6. The Bethe sequence therefore is retained only as an *upper*

bound on topological reach in liquid water, consistent across DIST and ANG. Each finite reference graph in Table 3 saturates at its total vertex count once BFS has visited every node (diamond-cubic and random 4-regular at ∼128); the plateau in those rows at large n reflects this finite-size saturation, not any feature of the H-bond network.

Table 3. Cumulative Bethe-tree shell sizes (theory, $z = 4$) versus BFS shell sizes computed from a diamond-cubic lattice, a random 4-regular graph, and an MD simulation of liquid water with two H-bond definitions (DIST and ANG). The measured reach $N_{\mathrm{MD}}(n)$ falls increasingly below the loop-free $z = 4$ tree as n grows; as discussed in the text this shortfall is largely a coordination-counting effect ($\langle z \rangle \approx 3.63$ rather than 4).

Shell n	0	1	2	3	4	5	6
Bethe theory ($z = 4$, infinite)	1	5	17	53	161	485	1457
Diamond cubic (128 vertices)	1	5	17	41	77	109	123
Random 4-regular (128 vertices)	1	5	16	45	96	127	128
TIP4P/Ew DIST	1.0	5.7	19.8	51.4	109.7	204.0	343.7
	±0.0	±0.0	±0.1	±0.3	±0.6	±1.1	±1.8
TIP4P/Ew ANG	1.0	4.6	14.3	35.4	74.7	139.3	236.5
	±0.0	±0.0	±0.1	±0.2	±0.4	±0.8	±1.4

The BFS analysis above is purely topological. A genuine band-resolved dynamical test of the participation bridge requires the mass-weighted instantaneous-normal-mode analysis of Sec. 5.3, presented next.

5.3. Dynamical test: instantaneous-normal-mode participation

We now test directly whether the band-resolved participation ratio $P_k = 1/\sum_i v_{ki}^4$ of the actual mass-weighted vibrational eigenvectors $\{v_k\}$ of liquid water matches the model hierarchy $N_{\mathrm{eff}} \in \{5, 53, 485\}$ at the corresponding intermolecular frequencies (180, 60, $\lesssim 30\,\mathrm{cm}^{-1}$). This is the direct dynamical-participation reading of the bridge, distinct from the topological reading tested in Sec. 5.2. Note that the three band frequencies (180, 60, $\lesssim 30\,\mathrm{cm}^{-1}$) are fixed by experiment and by the measured VDOS (Appendix B), not by the ladder, and P_k is measured directly on the INM eigenvectors at those frequencies. The $\tau \propto \sqrt{N_{\mathrm{eff}}}$ scaling only labels which shell each band is compared against and does not enter the measured P_k. So, whether P_k agrees with $N(n)$, is an independent empirical comparison.

The test is restricted to the three *odd-numbered* shells ($n = 1, 3, 5$) because only those map onto separately resolvable far-infrared/THz *bands* of liquid water (Table 2): the H-bond stretch ($\sim 180\,\mathrm{cm}^{-1}$), the H-bond bend ($\sim 60\,\mathrm{cm}^{-1}$), and the low-frequency connectivity band ($\lesssim 30\,\mathrm{cm}^{-1}$). The even shells 2, 4, 6 are time-domain ultrafast kinetic processes (vibrational relaxation, H-bond breaking, molecular-jump reorientation) with no isolatable spectral peak, and the INM test — which bins eigenvectors by frequency and averages $\langle P_k \rangle$ per window — is meaningful only for distinct, well-separated bands. The three odd shells also span the full range the linear bridge predicts ($N = 5 \to 53 \to 485$, a factor of ~ 100), giving maximum discriminating power; inserting the even shells would add intermediate points without changing the outcome.

Using the translational INM spectrum of Sec. 5.1 (eight frames of the production $N = 5000$ system), we sorted the modes into the three target frequency bands (180, 60, and $\lesssim 30\,\mathrm{cm}^{-1}$) and report the average participation ratio $\langle P_k \rangle$ in each band. As a basic sanity check, the vibrational density of states peaks near 150–200 cm^{-1}, consistent with the published INM literature for liquid water [18,19].

Table 4 compares the measured band-averaged participation ratios with the model values. The measured $\langle P_k \rangle$ increase only modestly across the three bands, in contrast to the steep linear sequence $5 \to 53 \to 485$: the translational-INM values run from

$\langle P_k \rangle \approx 677$ at the 180 cm^{-1} band to ≈ 1317 at the $\lesssim 30\,\mathrm{cm}^{-1}$ band. The standard errors are small on this scale (Table 4), so even the lowest-frequency band, pooled over 1668 modes, already spreads over more than 485 molecules. A separate rigid-body $6N$ cross-check that includes molecular rotations gives an even flatter profile (Table 4); in both analyses the band-to-band variation is at most a factor of two. This is the central measurement of the participation content of the ladder: the low-frequency intermolecular modes are delocalised, so the participation saturates with frequency rather than tracking the shell sizes $N(n)$. The saturating profile is exactly what the delocalisation-saturated law given by Eq. (16) describes. The modest variation of $\langle P_k \rangle$ also measures the role of the equal-amplitude assumption underlying the $\tau \propto \sqrt{N_{\mathrm{eff}}}$ scaling (Sec. 2.4(b)): most of the shell-to-shell change is carried by a shell-dependent restoring stiffness $k(n)$ rather than by the participation count, so the equal-amplitude reading is a simplification of the measured stiffness behaviour.

The rotation-included $6N$ Hessian already contains the molecular librations, so binning its modes by frequency probes the most prominent far-IR feature above the translational window (the librational band near 720 cm^{-1}). At ambient density the librational continuum (400–800 cm^{-1}) still participates over $\langle P_k \rangle \approx 1925$ molecules ($\approx 0.39\,N$), and a finer frequency-resolved decomposition (Appendix C) confirms that participation falls smoothly toward the high-frequency edge but remains delocalised over $\sim 10^3$ molecules even in the librational band. Frequency-resolving the spectrum therefore confirms the delocalisation directly: even the most localised intermolecular band of liquid water spreads over many molecules, consistent with the saturating participation law established below.

The apparent paradox of comparing $N(1) = 5$ with a measured $P_k \approx 677$ is the cleanest statement of the result: the two are different *kinds* of object. $N(1) = 5$ is an *intensive* topological count (a molecule plus its four neighbours, independent of system size), whereas P_k is an *extensive* dynamical quantity that grows with the box ($P \sim O(N)$ for delocalised modes, with only the spectral tails localising [19,39]). The linear reading would make the 180 cm^{-1} band a compact five-molecule breathing mode; the data show a *delocalised* network mode spread over $\sim 0.14\,N$ molecules. These are therefore delocalised network modes, so the meaningful size-independent comparison is the band-to-band participation *ratio*, normalised to the 180 cm^{-1} band, which is invariant under a change of box size.

On this common axis the participation law is read off directly (Fig. 3(b)). The *linear* reading $N_{\mathrm{eff}}(n) = N(n)$ would give a steeply rising profile $1 : 10.6 : 97$; the translational INM data give a flat $1 : 1.93 : 1.95$ (from $677 : 1303 : 1317$) and the rigid-body $6N$ data $1 : 1.01 : 1.01$ (from $2379 : 2404 : 2404$). The measured profile is therefore flat, establishing that participation saturates: the departure from the steep linear profile is much larger than the inter-frame scatter, and it remains clear even under deliberately inflated uncertainty estimates. Thus the compact linear bridge $N_{\mathrm{eff}}(n) = N(n)$ is not validated as the actual participation law of liquid water. This measured saturation is exactly the behaviour the delocalisation-saturated law given by Eq. (16) captures; the MD replaces the compact-cluster participation reading with a phenomenological saturated participation law while leaving the empirical frequency placements as a separate organizing step.

Figure 3(b) shows the same result geometrically. The measured curve starts far above the $P_k = N$ line at small assigned shell size ($\langle P_k \rangle \approx 342$ at $N \approx 3$) and then rises only modestly, reaching ≈ 1330 at $N \approx 600$. The participation law is therefore saturating rather than linear: the absolute values show delocalised modes, and the band-to-band ratios give the size-independent summary of that saturation.

As an independent confirmation, we project the time series of oxygen-atom velocities onto the model's predicted shell-1 vibrational pattern (the central molecule moving against

the mean velocity of its four H-bonded neighbours) and compute the resulting frequency spectrum. The cross-check is now fully specified. For each of 273 central molecules we built the shell-1 displacement pattern at the instantaneous H-bond geometry — the root oxygen velocity minus the mean velocity of its four nearest H-bonded neighbours — normalised it to unit Euclidean norm, projected the oxygen-velocity trajectory onto it, and formed the power spectral density (PSD) of the scalar projection; the 273 single-molecule PSDs were then averaged. The unprojected reference is the PSD of the raw oxygen velocities over the same molecules and frames, so the comparison is the dimensionless ratio of integrated band powers, projected over unprojected, in each target window. If the shell-1 pattern were a dynamically distinguished direction, this ratio would exceed unity at 180 cm^{-1}. We find no significant amplification: the integrated-power ratio is 1.06 (+5.9%) in the 180 cm^{-1} band (120–240 cm^{-1}), 0.99 (−0.8%) at 60 cm^{-1}, and 0.88 (−11.7%) below 30 cm^{-1}. The noise floor, estimated from the scatter of the same ratio across four control windows between 240 and 720 cm^{-1} (where the shell-1 direction should produce no enhancement), is $\sigma \approx 4\%$; the +5.9% enhancement at 180 cm^{-1} is therefore only $\approx 1.5\sigma$ and consistent with zero, while the lower bands show no enhancement at all. Because this projection uses a limited set of central molecules and a simple control-window noise estimate, we treat it only as a supporting null check, not as an independent statistical rejection test. The shell-1 spatial pattern is thus not a special direction of the actual vibrational motion in the H-bond stretch region, in agreement with the INM participation result above.

Table 4. Mass-weighted INM participation ratios in the production $N = 5000$ TIP4P/Ew system at ambient density ($\rho \simeq 1.0\,\mathrm{g\,cm}^{-3}$, 298 K), compared with the model's predicted N_{eff} values. Translational rows: Hessian of the molecular centre-of-mass translations, 8 instantaneous thermal frames (120,000 modes pooled); the three bands are 120–240, 40–90, and 2–30 cm^{-1}. The SEM column is the standard error across the 8 independent frames. The final row adds the rotation-included rigid-body $6N$ cross-check (4 frames, 120,000 modes; band-averaged participations), which is even flatter. The last two columns give the system-size-*independent* comparison: the fractional participation $\langle P_k \rangle / N$, and the band-to-band ratio normalised to the 180 cm^{-1} band. The model requires this ratio to climb 1 : 10.6 : 97; the data stay within a factor of 2 (translational) or $\sim 1\%$ ($6N$), with the modes occupying a roughly band-independent fraction of the whole box.

Band	N_{modes}	$\langle P_k \rangle$	SEM	model N_{eff}	$\langle P_k \rangle / N$	ratio /180
180 cm^{-1} (H-bond stretch)	39936	677	±3.7	5	0.135	1.00
60 cm^{-1} (H-bond bend)	11389	1303	±3.5	53	0.261	1.93
$\lesssim$ 30 cm^{-1} (connectivity)	1668	1317	±13.7	485	0.263	1.95
model prediction	—	$5 \to 485$	—	$5 \to 485$	—	1:10.6:97
$6N$ rigid-body (rot.+trans.), band-avg.	120000	$2379 \to 2404$	±3–5	$5 \to 485$	0.48	$1.00 \to 1.01$

5.4. What the two tests establish

The two tests establish complementary facts about the participation content of the ladder. The *topological* reading is a clean bound: the loop-free Bethe sizes upper-bound the BFS reach of any network of the same valence, and the measured reach $N_{\mathrm{MD}}(n)$ tracks that bound until ordinary $\langle z \rangle \approx 3.63$ coordination (rather than ring physics) opens a gap (Sec. 5.2); $N_{\mathrm{MD}}(n)$ thus describes the connectivity of the network. The *dynamical* reading is the decisive measurement: it shows that participation saturates, with the band-to-band ratio staying within a factor of ~ 2 instead of climbing the steep linear 1 : 10.6 : 97, and the delocalisation-saturated bridge given by Eq. (16) reproduces the frequency-resolved participation curve with a coherence cutoff $N_* \approx 7$ (twelve frequency points; Table 5). The shell-1 mode-projection cross-check agrees: there is no preferred-direction amplification, because beyond the first coordination shell the breathing motion is shared with the surrounding network.

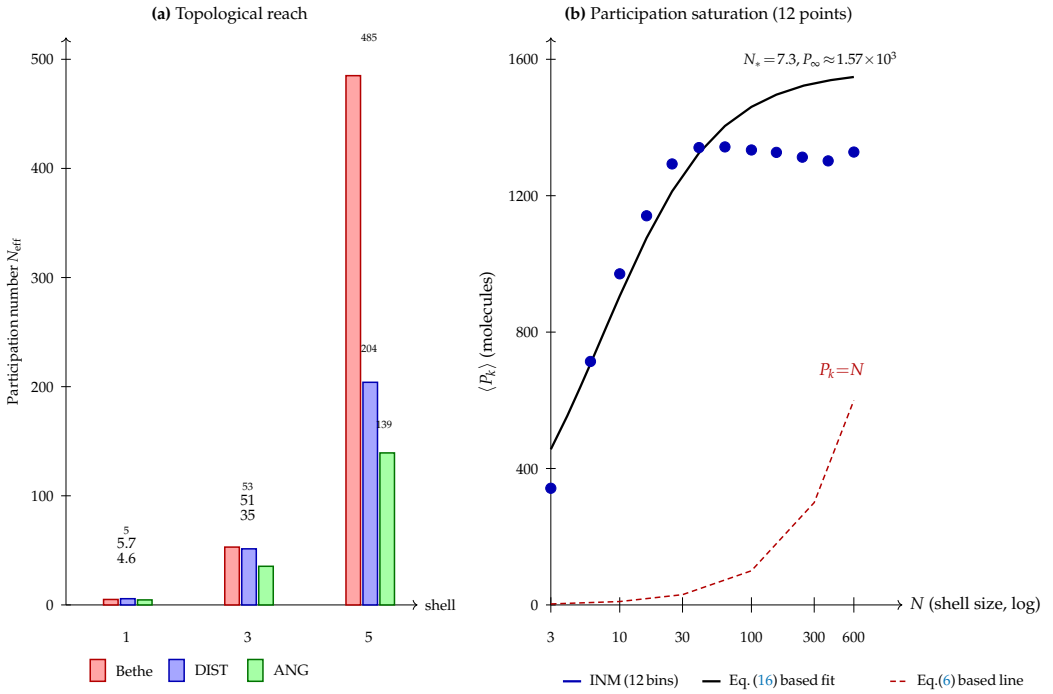

Figure 3. Topology and dynamics of the Bethe-shell participation-number interpretation. **(a)** BFS reach in the actual H-bond graph at shells 1, 3, and 5 under both DIST and ANG H-bond definitions, compared with the Bethe upper bound (red bars). **(b)** The dynamical test as a participation-saturation curve over twelve frequency-resolved points (production $N = 5000$, 298 K; the same data tabulated in Table 5). The band-averaged participation $\langle P_k \rangle$ (blue points) is plotted against the cluster size N assigned to each frequency window by the φ-ladder, on a logarithmic N axis. The *linear* bridge given by Eq.(6) (red dashed, $P_k = N$) would have participation track the cluster count; the data instead saturate at a band-limited plateau, and the delocalisation-saturated corrected bridge given by Eq. (16) [deep-pink curve, joint fit $N_* = 7.3 \approx N(1)$, $P_\infty \approx 1.57 \times 10^3$], captures the rise-then-plateau shape across the whole band. The participation spans only a factor of ~ 4 over the resolvable range, and Table 4 gives the corresponding band-to-band ratios (1 : 1.93 : 1.95 measured versus 1 : 10.6 : 97 for the linear count).

5.5. The corrected participation bridge: a delocalisation-saturated law $N_{\mathrm{eff}} = F(N(n))$.

The identification $N_{\mathrm{eff}}(n) = N(n)$ in Eq.(6) is the small-cluster limit: it equates the dynamical participation number with a loop-free topological count, and it holds while a shell-n in-phase breathing motion stays coherent over all $N(n)$ molecules. The molecular-dynamics test of Sec. 5.3 shows that this coherence is limited, so we promote Eq.(6) to a bridge that keeps the topological index $N(n)$ as the independent variable but accounts for the finite coherence range of a real network. An in-phase shell vibration can stay coherent only over a limited number of molecules, N_*. For clusters larger than N_* the motion mixes with the many extended vibrations of the surrounding network, so the number of molecules sharing it stops growing with the nominal cluster size and levels off at a plateau P_∞ (set by the band and the box size). We use the following Padé-like one-crossover form as the simplest phenomenological interpolation between these limits, not as a unique derivation from first principles:

$$N_{\mathrm{eff}}(n) \;=\; F\big(N(n)\big) \;=\; \frac{P_\infty\, N(n)}{N(n) + N_*}, \tag{16}$$

which interpolates between a *localised* regime, $N_{\mathrm{eff}} \simeq (P_\infty/N_*)\, N(n)$ when $N(n) \ll N_*$ (linear in the shell count — the original bridge Eq.(6), valid only near the first shell), and a *delocalised* regime, $N_{\mathrm{eff}} \to P_\infty$ when $N(n) \gg N_*$ (participation saturates, independent of n). Equation (16) is the corrected bridge Eq. (16); the old Eq.(6) is its small-cluster tangent. To constrain the two parameters we do not rely on the three named bands alone — a two-parameter law fitted to three points would be weakly determined — but fit the *frequency-resolved* participation curve of the production-run TIP4P/Ew translational INM spectrum (69,241 stable modes from eight $N = 5000$ frames at ambient density $\rho \simeq 1.0\,\mathrm{g\,cm^{-3}}$, binned into twelve logarithmically spaced windows from 15 to 225 $\mathrm{cm^{-1}}$ and each window centre assigned a continuous shell size N through the φ-ladder frequency–rung map; Table 5). The joint fit over all twelve points gives

$$N_* \;\approx\; 7.3 \text{ (twelve points; three-band fit: 4.9)}, \qquad P_\infty \;\approx\; 1.6 \times 10^3. \tag{17}$$

Both estimates of N_* are of order the first-shell count $N(1) = 5$ — i.e. a few molecules, one coordination shell — which is the physically meaningful statement; the two fits agree on that order of magnitude rather than on a precise value. with a root-mean-square residual of 16% over the twelve points (Table 5). The participation rises from $\langle P_k \rangle \approx 342$ at the high-frequency edge to a plateau near 1330 — a factor-of-$\sim$4 spread across the resolvable band, not the factor of $\sim$100 the linear bridge demands. With twelve points the two-parameter law is over-determined, so the close-but-imperfect fit is a genuine test of the functional form rather than an interpolation through a handful of values; the larger residual relative to a coarse three-band fit (which returns $N_* = 4.9$ at 3%, of the same order — one coordination shell) is the honest price of that over-determination, and the core, model-independent content is the flat band ratio of Sec. 5.3, which the fit then summarises as a saturating law. Two features make the fitted parameters physically interpretable. First, the crossover scale comes out at $N_* \approx N(1)$, i.e. *one coordination shell*: coherent shell-breathing survives up to the first neighbour cage and no further, which is exactly where the localised-cluster picture should break down. Second, the rotation-included $6N$ modes, which couple librations into every band, are even more strongly delocalised and give $N_* \to 0$ (saturated at all shells). We are explicit that P_∞ is an *extensive* quantity ($\approx 0.31\, N_{\mathrm{tot}}$ here) and is therefore calibrated, not predicted; the transferable, system-size-independent content of Eq. (16) is the crossover *shape* and the crossover scale N_*.

The linear bridge $N_{\mathrm{eff}}(n) = N(n)$, Eq.(6), was first proposed as the mechanism linking network topology to the ladder spacing (topology $\to$ participation $\to$ rung spacing, via

Table 5. Frequency-resolved test of the delocalisation-saturated bridge, Eq. (16). The pooled $N = 5000$ TIP4P/Ew translational INM spectrum (ambient density, 298 K, eight frames) is binned into twelve logarithmically spaced windows: $\tilde{\nu}$ is the window centre, N the continuous Bethe shell size assigned by the φ-ladder frequency–rung map, $\langle P_k \rangle$ the band-averaged participation, and $F(N)$ the corrected-bridge value at the joint best fit $N_* = 7.3$, $P_\infty = 1.57 \times 10^3$ (rms 16% over all twelve points).

$\tilde{\nu}$ (cm^{-1})	N	$\langle P_k \rangle$	$F(N)$
14.7	600	1328	1548
18.9	383	1302	1538
24.2	244	1313	1521
31.0	155	1327	1497
39.7	99	1334	1459
50.9	63	1343	1403
65.2	40	1341	1323
83.5	25	1293	1212
107	16	1141	1066
137	10	971	888
176	6	714	690
225	3	342	488

$\tau \propto \sqrt{N_{\text{eff}}}$). The molecular dynamics do not confirm that mechanism for the actual liquid. They refine this picture: the low-frequency modes are delocalised, so the participation numbers saturate at about one coordination shell rather than growing like $N(n)$, and the MD-calibrated saturating law Eq. (16) gives the participation content of each rung directly. The mapping of frequencies onto the ladder is, by contrast, unaffected, and nothing in the MD result bears on it: the rung spacing is set by the external geometric input φ, while the MD now supplies the participation law that populates each rung. The discrete ladder therefore stands as a calibrated organizing scheme for the band centres, with its spacing fixed externally and its participation content measured.

5.6. Robustness: temperature

Within TIP4P/Ew, the measured participation law is stable over the two temperatures tested. Lowering the temperature from 298 to 277 K (near the experimental density maximum) leaves the translational band-to-band ratio (1:1.86:1.88 versus 1:1.93:1.95) little changed and the twelve-point coherence cutoff barely shifted ($N_* = 6.6$ versus 7.3; Table 6). More fundamentally, the saturation rests on a model-independent fact — delocalised network modes scale extensively, so the band-to-band ratio stays of order unity, which is generic to disordered harmonic networks.

Table 6. Temperature robustness of the translational INM participation result for TIP4P/Ew at ambient density ($N = 5000$, constant-pressure equilibration). Columns give the band-averaged participation ratios, the band-to-band ratio normalised to the 180 cm^{-1} band, the coherence cutoff N_* from the twelve-point corrected-bridge fit [Eq. (16)], and the residual.

Run	$\langle P \rangle_{180}$	$\langle P \rangle_{60}$	$\langle P \rangle_{<30}$	ratio (norm. 180)	N_*	rms %
298 K (production)	677	1303	1317	1:1.93:1.95	7.3	16.0
277 K	712	1326	1339	1:1.86:1.88	6.6	10.9
linear bridge $N(n)$	5	53	485	1:10.6:97	—	—

6. Open questions and outlook

Two theoretical problems are left open by the present model. First, the $T_c \to T_{\max}$ broadening factor of Eq. (15) still needs a microscopic equation-of-state derivation. Second, the residual ring contribution to the BFS reach shortfall would acquire predictive status

only if it could be derived independently — e.g. via a branching reference built from rings rather than single bonds (a "Husimi tree"), which would explicitly include the 5- and 6-membered rings that dominate liquid water [11].

Three experimental tests remain outstanding; each is stated below as a single case, together with what it can and cannot establish.

Test (i): band-resolved mode participation. An *experimental* measurement of band-resolved mode participation — e.g. via isotope-dilution or spatially resolved THz probes — to complement the simulations. This test directly checks the measured participation law: it states a prediction in advance (a compressed, factor-of-a-few participation spread), and the measurement would either confirm or revise the saturating law established in Sec. 5.3. At the present precision, a normalised band-to-band participation ratio outside roughly $(0.5, 2.0)$ would falsify the compressed-ratio version of the law.

Test (ii): librational-edge T_c reporter. The temperature dependence of the librational-continuum edge at $\sim$ 720–730 cm^{-1} could be tested as a possible reporter of the same near-freezing network change. This is a consistency check: a confirmed T_c reporter would be supportive but, given the calibrated status of the thermodynamic mapping (Sec. 4), could not by itself upgrade that mapping to a prediction.

Test (iii): confinement deviation of $T_{max} - T_c$. A confinement experiment could test whether $(T_{max} - T_c)/T_c$ departs from the bulk-water $\varphi^{-8} \approx 0.02$ ratio of Eq. (15) in hydrophobic nanopores; the cleanest version would require an independent estimate that the effective H-bond energy scale E_{coh} is not strongly shifted by confinement [54]. This is a prediction stated in advance for a future experiment: it specifies a measurable deviation of the $T_{max} - T_c$ relation under confinement, and a null result constrains only that relation, not the ladder.

A fourth, purely computational test is also important: a direct model-selection or randomisation analysis of the rung placements against nearby logarithmic bases, and an independent-water-model repeat of the INM participation analysis. These checks would determine how much of the present bracketing is specific to φ and how much of the measured saturation is force-field independent.

7. Conclusion

This work connects three quantities for liquid water within one calibrated golden-ratio construction: the ultrafast and far-infrared/terahertz band placements, the near-freezing temperature map, and the molecular-dynamics participation law. The construction is intentionally presented as a calibrated organizing framework, not as proof that liquid water uniquely selects φ or as a derived equation of state. Three results stand out.

First, the principal hydrogen-bond timescales and the far-IR/THz intermolecular band centres can be placed *together* on one discrete golden-ratio (φ) ladder, anchored to the 80 fs H-bond contraction time and indexed by the loop-free tetrahedral Bethe sequence: each observable falls inside the rung window set by its shell index (Sec. 3). This paper demonstrates the common placement explicitly: the time-domain ultrafast set and the frequency-domain THz/far-IR set are organized on the same φ-spaced rung scheme from one time anchor, subject to the half-rung windows and anchor uncertainty stated above.

Second, the same golden-ratio factor maps the two experimentally observed thermal landmarks of liquid water. With the separate energy calibration stated in Sec. 4, the ladder recovers both the freezing point and the temperature of maximum density, with the small offset between them following the $\varphi^{-8} \approx 0.02$ rung spacing. One φ-based relation thus links the molecular timescale ladder to the macroscopic density anomaly at the phenomenological level.

Third, and most quantitatively, a TIP4P/Ew instantaneous-normal-mode test measures the participation content associated with the ladder. The measured band-resolved participation follows a delocalisation-saturated law $N_{\mathrm{eff}}(n) = P_\infty\, N(n)/[N(n) + N_*]$ with a coherence cutoff N_* of about one coordination shell — a result that is consistent across the two tested temperatures, 298 and 277 K. The shell-1 velocity-projection check gives no positive dynamical signature at the assigned 180 cm^{-1} band within its $\sim 4\%$ noise floor, so the bridge is supported by participation ratios rather than by a distinct velocity-correlation enhancement. This establishes a calibrated, physically interpretable bridge between network topology and vibrational participation, with the φ ladder supplying the rung spacing and the molecular dynamics supplying the participation law that populates it.

Author Contributions: J.W.: Project administration; Conceptualization; Writing, original draft. **E.A.:** Conceptualization; Molecular-dynamics simulations (Software, Investigation, Data curation); Writing, review & editing. Both authors contributed to the methodology, formal analysis and final manuscript. All authors have read and agreed to the published version of the manuscript.

Funding: This research received no external funding.

Acknowledgments: The authors thank the OpenMM developers for the simulation toolkit used in the molecular-dynamics tests of Sec. 5.2–5.4. No external funding was used.

Conflicts of Interest: The authors declare no financial or professional conflicts of interest related to this work.

Appendix A Intramolecular vibrations: rung placements

The intramolecular O–H stretch ($\sim$ 10 fs) and H–O–H bend ($\sim$ 1640 cm^{-1}, $\sim$ 20 fs) are not shell-n network modes of the Bethe construction, because they involve no H-bond network topology. They are excluded from the ladder-performance claims; here we only record where they would fall if placed on the same φ-ladder. These placements are bookkeeping only and are not counted as evidence for the network ladder.

For the O–H stretch, rung 1 ($\sim$ 10 fs) is not a Bethe-shell vibration. The φ^8 that appears here is a *stiffness* ratio, not a rung index, and follows in two steps. (1) Rung 1 sits four rungs below the rung-5 anchor, and each rung is one factor of φ in period, $\tau_r = \tau_5\, \varphi^{r-5}$, so $\tau_1 = 80\,\mathrm{fs} \times \varphi^{-4} \approx 11\,\mathrm{fs}$ (the $\sim$3400 cm^{-1} stretch) and the rung-5-to-rung-1 period ratio is φ^4. (2) In the harmonic model of Sec. 2.4(b), at fixed effective mass $\omega = \sqrt{k/\mu} \propto 1/\tau$, so stiffness scales as the square of frequency: $k_1/k_5 = (\tau_5/\tau_1)^2 = (\varphi^4)^2 = \varphi^8 \approx 47$. This covalent-to-H-bond stiffness ratio falls inside the published range $\sim$ 15–90 [54,55]; because the range is broad and the mode is intramolecular, this comparison is not used as a ladder-performance check.

The H–O–H bend is the other intramolecular placement recorded here. It sits near the unused rung 2 and gives

$$\tau_{\mathrm{bend}} \;=\; \tau_0\, \varphi^2 \;\approx\; 18.9\,\mathrm{fs}, \qquad \tilde{\nu}_{\mathrm{bend}} \;\approx\; 1766\,\mathrm{cm}^{-1}. \tag{A18}$$

The obtained bend value is within about 8% of the observed liquid-water bend at $\sim$ 1640 cm^{-1} [12]; this is recorded only as a placement on the same ladder, not as evidence for a Bethe-shell network mode.

Appendix B Vibrational density of states of TIP4P/Ew water

The participation-bridge tests of Sec. 5 assign the shell-1 band to the experimentally observed $\sim$ 180 cm^{-1} H-bond stretch [7,9,10], so we check whether the TIP4P/Ew oxygen-velocity spectrum contains a corresponding VDOS feature. A separate fine-cadence trajectory (same force field, $N = 5000$, and protocol as Sec. 5.1, with velocities written

every 4 fs over 50 ps of NVE production) gives the bulk VDOS as the power spectrum of the oxygen-velocity autocorrelation, averaged over all 5000 oxygens.

In the 150–220 cm^{-1} window the simulated VDOS has two maxima, at 183 and 207 cm^{-1}, both inside the rung-6–7 window of Table 2: the 183 cm^{-1} peak aligns in frequency with the experimental H-bond-stretch band, while the 207 cm^{-1} peak is a TIP4P/Ew-specific feature. The simulation therefore contains the shell-1 spectral feature used in the tests of Sec. 5.2 and 5.3. The 20 ps record resolves $\sim 1.7\,cm^{-1}$, finer than the $\sim 5\,cm^{-1}$ structure of interest, and applying a Hann window shifts the 183 cm^{-1} peak by $< 2\,cm^{-1}$ without changing the assignment.

Appendix C Frequency-resolved rigid-body ($6N$) spectrum

Frequency-resolving the rigid-body $6N$ spectrum shows the libration–translation structure explicitly: participation falls smoothly from $\langle P_k \rangle \approx 2370$ (0.47 N) in the 0–150 cm^{-1} translational region to ≈ 1845 (0.37 N) at 500–700 cm^{-1} and ≈ 1064 (0.21 N) in the librational band (700–760 cm^{-1}), continuing to drop toward the high-frequency edge as expected for instantaneous-normal-mode localisation in the spectral tails [19,39].

References

1. J. D. Bernal and R. H. Fowler, *A theory of water and ionic solution, with particular reference to hydrogen and hydroxyl ions*, J. Chem. Phys. **1**(8), 515–548 (1933). doi: 10.1063/1.1749327.
2. L. Pauling, *The structure and entropy of ice and of other crystals with some randomness of atomic arrangement*, J. Am. Chem. Soc. **57**, 2680–2684 (1935). doi: 10.1021/ja01315a102.
3. F. H. Stillinger, *Water revisited*, Science **209**(4455), 451–457 (1980). doi: 10.1126/science.209.4455.451.
4. P. Wernet *et al.*, *The structure of the first coordination shell in liquid water*, Science **304**(5673), 995–999 (2004). doi: 10.1126/science.1096205.
5. A. K. Soper, *The radial distribution functions of water as derived from radiation total scattering experiments: is there anything we can say for sure?*, ISRN Physical Chemistry **2013**, 279463 (2013). doi: 10.1155/2013/279463.
6. L. B. Skinner *et al.*, *The structure of water around the compressibility minimum*, J. Chem. Phys. **141**, 214507 (2014). doi: 10.1063/1.4902412.
7. G. E. Walrafen, *Raman spectral studies of the effects of temperature on water structure*, J. Chem. Phys. **40**, 3249 (1964). doi: 10.1063/1.1724992.
8. H. R. Zelsmann, *Temperature dependence of the optical constants for liquid H_2O and D_2O*, J. Mol. Struct. **350**, 95 (1995). doi: 10.1016/0022-2860(94)08471-S.
9. J.-B. Brubach *et al.*, *Signatures of the hydrogen bonding in the infrared bands of water*, J. Chem. Phys. **122**, 184509 (2005). doi: 10.1063/1.1894929.
10. T. Fukasawa *et al.*, *Relation between dielectric and low-frequency Raman spectra of hydrogen-bond liquids*, Phys. Rev. Lett. **95**, 197802 (2005). doi: 10.1103/PhysRevLett.95.197802.
11. M. Matsumoto, A. Baba, and I. Ohmine, *Topological building blocks of hydrogen bond network in water*, J. Chem. Phys. **127**, 134504 (2007). doi: 10.1063/1.2772658.
12. J. E. Bertie and Z. Lan, *Infrared intensities of liquids XX: the intensity of the OH stretching band of liquid water revisited*, Appl. Spectrosc. **50**, 1047–1057 (1996). doi: 10.1366/0003702963905385.
13. C. J. Fecko *et al.*, *Ultrafast hydrogen-bond dynamics in the infrared spectroscopy of water*, Science **301**, 1698 (2003). doi: 10.1126/science.1087251.
14. D. Laage and J. T. Hynes, *A molecular jump mechanism of water reorientation*, Science **311**, 832–835 (2006). doi: 10.1126/science.1122154.
15. H. J. Bakker and J. L. Skinner, *Vibrational spectroscopy as a probe of structure and dynamics in liquid water*, Chem. Rev. **110**, 1498–1517 (2010). doi: 10.1021/cr9001879.
16. G. Giovannetti *et al.*, *Real-time tracking of the intramolecular vibrational dynamics of liquid water*, Commun. Chem. **9**, 57 (2026). doi: 10.1038/s42004-025-01863-x.
17. J. Yang *et al.*, *Direct observation of ultrafast hydrogen bond strengthening in liquid water*, Nature **596**, 531–535 (2021). doi: 10.1038/s41586-021-03793-9.

18. P. A. Madden and R. W. Impey, *On the infrared and Raman spectra of water in the region* $5-250\,cm^{-1}$, Chem. Phys. Lett. **123**(6), 502–506 (1986). doi: 10.1016/0009-2614(86)80027-9.
19. M. Cho *et al.*, *Instantaneous normal mode analysis of liquid water*, J. Chem. Phys. **100**, 6672–6683 (1994). doi: 10.1063/1.467027.
20. W. L. Jorgensen *et al.*, *Comparison of simple potential functions for simulating liquid water*, J. Chem. Phys. **79**, 926–935 (1983). doi: 10.1063/1.445869.
21. J. L. F. Abascal and C. Vega, *A general purpose model for the condensed phases of water: TIP4P/2005*, J. Chem. Phys. **123**, 234505 (2005). doi: 10.1063/1.2121687.
22. B. Cheng, E. A. Engel, J. Behler, C. Dellago, and M. Ceriotti, *Ab initio thermodynamics of liquid and solid water*, Proc. Natl. Acad. Sci. USA **116**, 1110–1115 (2019). doi: 10.1073/pnas.1815117116.
23. P. H. Poole, F. Sciortino, U. Essmann, and H. E. Stanley, *Phase behaviour of metastable water*, Nature **360**, 324–328 (1992). doi: 10.1038/360324a0.
24. J. Russo and H. Tanaka, *Understanding water's anomalies with locally favoured structures*, Nature Commun. **5**, 3556 (2014). doi: 10.1038/ncomms4556.
25. H. Tanaka, *Liquid–liquid transition and polyamorphism*, J. Chem. Phys. **153**, 130901 (2020). doi: 10.1063/5.0021994.
26. M. Heyden, J. Sun, S. Funkner, G. Mathias, H. Forbert, M. Havenith, and D. Marx, *Dissecting the THz spectrum of liquid water from first principles via correlations in time and space*, Proc. Natl. Acad. Sci. USA **107**, 12068 (2010). doi: 10.1073/pnas.0914885107.
27. G. Stell and P. C. Hemmer, *Phase transitions due to softness of the potential core*, J. Chem. Phys. **56**, 4274–4286 (1972). doi: 10.1063/1.1677857.
28. A. Geiger, F. H. Stillinger, and A. Rahman, *Aspects of the percolation process for hydrogen-bond networks in water*, J. Chem. Phys. **70**, 4185–4193 (1979). doi: 10.1063/1.438042.
29. V. Holten and M. A. Anisimov, *Entropy-driven liquid–liquid separation in supercooled water*, Sci. Rep. **2**, 713 (2012). doi: 10.1038/srep00713.
30. P. G. Debenedetti, F. Sciortino, and G. H. Zerze, *Second critical point in two realistic models of water*, Science **369**, 289–292 (2020). doi: 10.1126/science.abb9796.
31. K. H. Kim *et al.*, *Experimental observation of the liquid–liquid transition in bulk supercooled water under pressure*, Science **370**, 978–982 (2020). doi: 10.1126/science.abb9385.
32. T. Isogai, M. Uranagase, K. Motobayashi, S. Ogata, and K. Ikeda, *Probing collective terahertz vibrations of a hydrogen-bonded water network at buried electrochemical interfaces*, Chem. Sci. **14**, 6531 (2023). doi: 10.1039/D3SC01734F.
33. A. Leitenstorfer *et al.*, *The 2023 terahertz science and technology roadmap*, J. Phys. D: Appl. Phys. **56**, 223001 (2023). doi: 10.1088/1361-6463/acbe4c.
34. P. Ren and J. W. Ponder, *Polarizable atomic multipole water model for molecular mechanics simulation*, J. Phys. Chem. B **107**, 5933 (2003). doi: 10.1021/jp027815+.
35. X. Zhu, M. Riera, E. F. Bull-Vulpe, and F. Paesani, *MB-pol(2023): Sub-chemical accuracy for water simulations from the gas to the liquid phase*, J. Chem. Theory Comput. **19**, 3551 (2023). doi: 10.1021/acs.jctc.3c00326.
36. V. Babin, C. Leforestier, and F. Paesani, *Development of a "first principles" water potential with flexible monomers*, J. Chem. Theory Comput. **9**, 5395 (2013). doi: 10.1021/ct400863t.
37. G. R. Medders, V. Babin, and F. Paesani, *Development of a "first principles" water potential with flexible monomers. III. Liquid phase properties*, J. Chem. Theory Comput. **10**(8), 2906–2910 (2014). doi: 10.1021/ct5004115.
38. C. Faccio, M. Benzi, L. Zanetti-Polzi, and I. Daidone, *Low- and high-density forms of liquid water revealed by a new medium-range order descriptor*, J. Mol. Liq. **355**, 118922 (2022). doi: 10.1016/j.molliq.2022.118922.
39. B.-C. Huang and C.-H. Chang, *Localization–delocalization transition of the instantaneous normal modes of liquid water*, Phys. Rev. E **88**, 042116 (2013). doi: 10.1103/PhysRevE.88.042116.
40. D. C. Elton and M.-V. Fernández-Serra, *The hydrogen-bond network of water supports propagating optical phonon-like modes*, Nat. Commun. **7**, 10193 (2016). doi: 10.1038/ncomms10193.
41. J. Washburn and M. Zlatanović, *Uniqueness of the canonical reciprocal cost*, Mathematics **14**(6), 935 (2026). doi: 10.3390/math14060935.
42. J. Washburn, M. Zlatanović, and E. Allahyarov, *Recognition geometry*, Axioms **15**(2), 90 (2026). doi: 10.3390/axioms15020090.

43. S. Pardo-Guerra, A. Thapa, M. Simons, and J. Washburn, *Coherent comparison as information cost: axiomatic foundations for discrete ledger dynamics*, Foundations **6**(2), 17 (2026). doi: 10.3390/foundations6020017.
44. M. Simons, E. Allahyarov, and J. Washburn, *A discrete informational framework for classical gravity: ledger foundations and galaxy rotation curve constraints*, Entropy **28**, 477 (2026). doi: 10.3390/e28040477.
45. J. Washburn, M. Zlatanović, and E. Allahyarov, *The d'Alembert inevitability theorem*, Mathematics **14**(8), 1386 (2026). doi: 10.3390/math14081386.
46. S. J. Suresh and V. M. Naik, *Hydrogen bond thermodynamic properties of water from dielectric constant data*, J. Chem. Phys. **113**, 9727–9732 (2000). doi: 10.1063/1.1323744.
47. E. D. Isaacs *et al.*, *Covalency of the hydrogen bond in ice: a direct X-ray measurement*, Phys. Rev. Lett. **82**, 600–603 (1999). doi: 10.1103/PhysRevLett.82.600.
48. M. Henry, *The hydrogen bond*, Inference: International Review of Science **6**(3) (2022).
49. H. W. Horn, W. C. Swope, J. W. Pitera, J. D. Madura, T. J. Dick, G. L. Hura, and T. Head-Gordon, *Development of an improved four-site water model for biomolecular simulations: TIP4P-Ew*, J. Chem. Phys. **120**, 9665 (2004). doi: 10.1063/1.1683075.
50. P. Eastman, J. Swails, J. D. Chodera, R. T. McGibbon, Y. Zhao, K. A. Beauchamp, L.-P. Wang, A. C. Simmonett, M. P. Harrigan, C. D. Stern, R. P. Wiewiora, B. R. Brooks, and V. S. Pande, *OpenMM 7: Rapid development of high performance algorithms for molecular dynamics*, PLOS Comput. Biol. **13**(7), e1005659 (2017). doi: 10.1371/journal.pcbi.1005659.
51. C. R. Harris *et al.*, *Array programming with NumPy*, Nature **585**, 357–362 (2020). doi: 10.1038/s41586-020-2649-2.
52. P. Virtanen *et al.*, *SciPy 1.0: Fundamental algorithms for scientific computing in Python*, Nat. Methods **17**, 261–272 (2020). doi: 10.1038/s41592-019-0686-2.
53. A. Luzar and D. Chandler, *Hydrogen-bond kinetics in liquid water*, Nature **379**, 55 (1996). doi: 10.1038/379055a0.
54. J. N. Israelachvili, *Intermolecular and Surface Forces*, 3rd ed., Academic Press (2011).
55. L. Pauling, *The Nature of the Chemical Bond and the Structure of Molecules and Crystals: An Introduction to Modern Structural Chemistry*, 3rd ed., Cornell University Press, Ithaca, NY (1960).